



## Original Article

# Evaluation of Several Austenitic Types of Stainless Steel's Chemical Corrosion Resistance

Hala. M. Hassan\*

Chemistry Department, Faculty of Science, Jazan University, KSA

## ARTICLE INFO

## Article history

Submitted: 2023-09-19

Revised: 2023-10-30

Accepted: 2023-11-08

Manuscript ID: CHEMM-2310-1730

Checked for Plagiarism: Yes

Language Editor:

Dr. Fatimah Ramezani

Editor who approved publication:

Dr. M. Selvaraj

DOI:10.48309/chemm.2023.421394.1730

## KEYWORDS

Stainless steel

Types

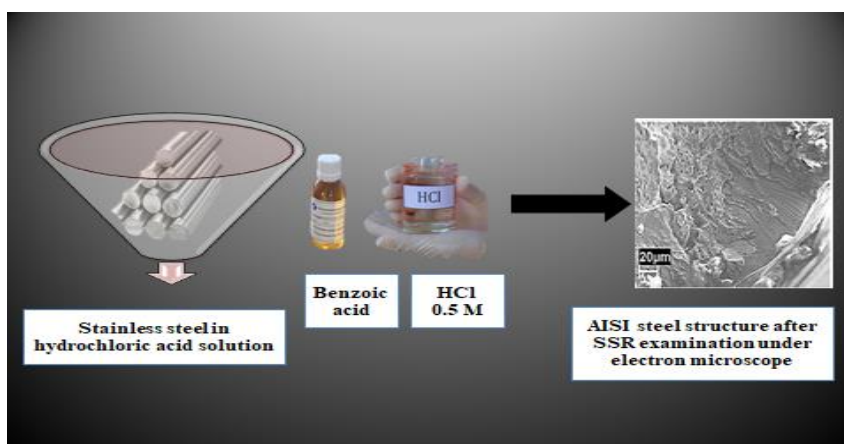
Chemical corrosion

Resistance

## ABSTRACT

This study aims to evaluate the efficacy of compounds as corrosion inhibitors for stainless steel in hydrochloric acid solution using gravimetric technique and electrochemical measurements. Stainless steel is resistant to corrosion and rust due to its chromium content, which reacts with oxygen in the air to form a protective coating. Passivation is the process of creating a thin layer of chrome oxide when exposed to oxygen, preventing rust. In this investigation, corrosion inhibitors made from benzoic acid derivatives were applied to 316 stainless steel in a 0.5 M hydrochloric acid solution. The outermost parts of the investigated stainless steel samples were examined using scanning electron microscopy and energy dispersive spectroscopy. The study also assessed the fundamental properties of the studied inhibitors using the dynamic molecular simulation method. The best inhibitor concentration for C3 at 291 K was 1.0 102 M, resulting in the highest inhibition efficiency (88%).

## GRAPHICAL ABSTRACT



\* Corresponding author: Hala. M. Hassan

✉ E-mail: [drhalahassan69@gmail.com](mailto:drhalahassan69@gmail.com)

© 2023 by SPC (Sami Publishing Company)

## Introduction

Equipped with an in-depth understanding of the physics driving interatomic relationships, molecular dynamic (MD) predictions forecast how each atom in a protein or other chemical system is going to change over time [1]. The examined organic substances exhibit strong connections with Fe and, as a result, have good corrosion-inhibiting capabilities for AISI 316 austenitic stainless steel (SS), according to the molecular dynamics modelling and diagnostics for molecule/metal association employed in this work. Weight loss experiments were used to determine the corrosion behaviour and rate of stainless steels. Using U-bend specimens, the susceptibility to stress corrosion cracking was assessed. Chemical issues are not just confined to exterior surfaces; austenitic stainless steels often offer the greatest corrosion resistance due to their high chromium content. Because of this, grade 304 is a great option when corrosion resistance is a concern. The different types of corrosion that can occur on stainless steels include uniform, pitting, crevice, intergranular, and stress corrosion cracking [2]. Depending on the total acid number (TAN), corrosion rates for carbon-steel or low-alloy steels containing chromium and molybdenum range from less than 1 mm/year to 4. They see insignificant erosion rates on austenitic stainless steels with 18% chromium without molybdenum (AISI 304) and with molybdenum (AISI 316); however, on ferritic stainless alloys with around 11.5% chromium in AISI 409, they observe corrosion rates that range between 0.1 and 0.8 mm/year. As opposed to stainless steels, the degree of hardness raises for carbon steels and aluminium alloys.

Because acidic substances are present, the pH was in the range of 3-3.5. Lead and iron showed high rates of corrosion; AISI 1045 carbon steel showed a somewhat lower rate, copper did not exhibit general corrosion, the significant volume of acidic water in aluminium produced severe corrosion to a lesser extent; and AISI 316 stainless steel showed virtually no corrosion. At

the current study, the prolonged structural behaviour that occurs in a eutectic  $\text{Li}_2\text{CO}_3\text{-Na}_2\text{CO}_3\text{-K}_2\text{CO}_3$  molten salt mixture at 600 °C in an air situation is evaluated and compared to that of AISI 301LN stainless steel, stainless double steel 2205 (DS2205), as well as better plex stainless 2507 (DS2507) for the first time. In addition to use complimentary microscopy as well as microanalysis techniques like X-ray diffraction and SEM to define the oxide scales that develop on the alloys, the chemical kinetics of the steels have been documented. The weathering process of these steels may be the cause of the adhesion of the oxide coverings to the metal a base, mechanical integrity, and surface roughness of these metals when they are in contact with molten salts [3]. Creep is the capacity to withstand the propensity to move slowly or deform when subjected to mechanical pressures. Austenitic stainless steels have exceptional corrosion resistance in a range of corrosion environments due to their high passivation capability. However, because of their poor hardness and great susceptibility to adhesive wear, these steels' characteristics are insufficient. Thermochemical procedures like nitriding or nitro carburizing can be utilised to enhance the wear behaviour of austenitic steels while preserving corrosion resistance. These operations can be carried out either separately or in conjunction with coating methods. By observing current density, potential curves, and conducting prolonged testing in corrosive environments, corrosion resistance was examined [4]. In actuality, AISI 316L was and AISI 304L steels, two popular steel alloy stainless steels, offer exceptional everywhere corrosion resistance owing to the development of passive coatings formed of chromium-rich oxide. The protective covering is resilient throughout a broad pH range while it is in the liquid phase. These types of steel are extensively used in both conventional and nuclear power plants due to their remarkable corrosion resistance and robust mechanical properties at high temperatures. After testing, a scanning electron microscope

analysis was done to look for fractures and specific attacks. In light of the exposure settings, the findings are discussed. They display very low amounts of corrosion that change with temperature as well as time, according to Mao *et al.* and Chiaberge *et al.* [3, 5].

## Experimental

### Materials and methods

#### Materials

Corrosion tests were performed on both AISI 316L and 304L, which stainless steels, which were purchased as 6 mm round bars or 1000 by 2000 mm<sup>2</sup> sheets with a 2.5-millimeter thickness. The alloy compositions are listed in Table 2. Oxalic acid etching was used to confirm the steel's microstructure in accordance with Normative Practise A of ASTM A262 for identifying intergranular attack vulnerable. In the absence of carbide precipitation at the grain boundary, both steels exhibit a "step" microstructure in Figures 1 and 2.

#### Sample preparation

Table 1 showed that atomic structure of steel molecules. SS301, a steel stainless-steel alloy with an AISI 301LN assessment equivalent to EN 1.4318, EN 1.4410 super flexible both directions stainless steel, which serves as an equivalent to UNS S32750, and the American Institute of Steel S31803 duplex stainless steel, supplied by UGINE and ALZ (Arcelor Mittal Group, Luxembourg City, Luxembourg), were the only readily available components that were reviewed.

#### Theoretical proportions of the metals

Either SS301 and DS2205 substances were supplied as bed linens, which were subsequently sliced to form prototypes with dimensions of forty x twenty and two millimeter three. DS2507, on the other hand, was marketed as a 20 mm wide bar that could be machined into cylinders with a 2-mm wall thickness. To remove the previously adherent metal oxide layers, 1200 grit Si C grind sheet (in pellets of Si C per square centimeter) was used to prepare the samples.

Following that, the collected specimens were weighed and cleaned in an ethanol-infused acoustic bath.

#### General corrosion tests

The fragments in issue were tested for rust by being immersed in molten salt at a temperature of 600 °C in conditions while they were within ovens constructed of alumina. Lithium carbonate by weight 99% (CAS No. 55413-2), potassium carbonate anhydrous LR (CAS No. 584-08-7), and magnesium carbonates anhydrous LR (CAS No. 497-19-8) were used to create the ideal mixture of Li<sub>2</sub>CO<sub>3</sub>-Na<sub>2</sub>CO<sub>3</sub>-K<sub>2</sub>CO<sub>3</sub> (32/33/35 wt%) at the melting temperature of 397 °C. Prior to that, every hydroxide salt had been air-dried in the oven for 48 hours at 180 °C employing an alumina crucible. The test rate was set to be greater than the point of melting of salt and the possibility for the development of stress corrosion cracking (SCC) by submerging U-bend specimens in pyrolysis oil at a temperature of 50 °C. On carbon and low-alloy steels, fractures were found after a period of 250 hours after exposure. Shallow cracks also appeared in stainless steel after exposures of 500 and 750 hours.

#### Chemical composition testing

The technique of X-ray spectroscopy without vitality displacement (EDX), another means of studying the substance of elements, was used in the test utilizing a Zeiss EVO 25 scanner electron microscope (SEM).

By collecting measurements on stations 300 x 300 m in dimensions, it was possible to become independent of specific ground morphological concerns and identify the measuring field as representative of the whole test field. At temperatures of around 600 °C, the composition of the work, such as vessel tanks, the gradual increase of the thicknesses decrease in metal with time spent in contact was fitted to a time-dependent power equation as follows to determine the rusting dynamics for each alloy:

Z's behaviour Equals  $ktn$ , in which the numbers  $k$  and  $n$  are the connecting parameters, denoting the rate constant and exponent, respectively, and  $z$  is the metal's wall thickness loss (measured in

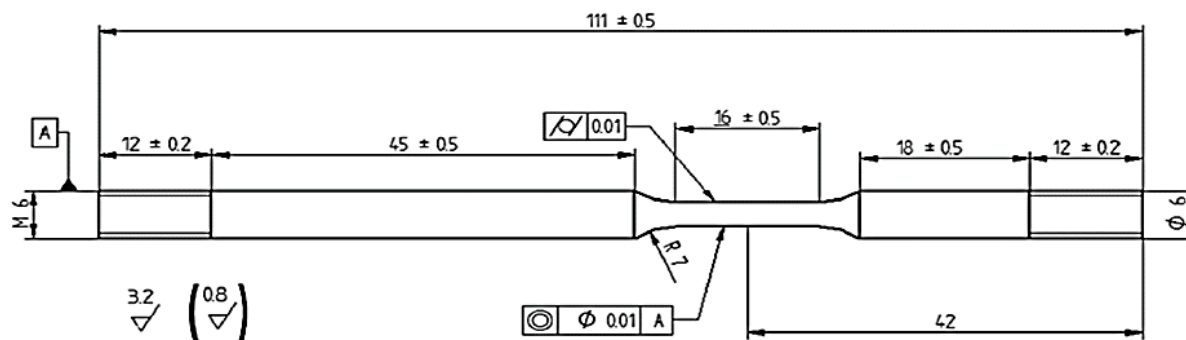


**Figure 1:** SSR geometry

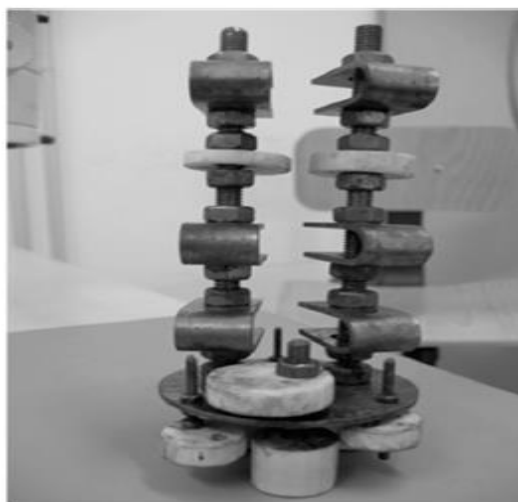


**Figure 2:** Specimen instrument

m) and  $t$  represents the exposure duration (measured in h).

An optical magnifying microscope (Olympus, Japan, Tokyo) overall a field-emitted scanning electron microscope (FESEM, Carl Zeiss Merlin, Oberkochen, Germany) were used to investigate the layer coating and metallic density. The loss of height of every alloy at different exposure durations (120, 300, 700, 1000, and 1300 h) was used to evaluate the corrosion behaviour. For the purpose of calculating the thickness loss for that exposure duration, at least 20 observations involving a pair of samples of each alloy were made. The loss of metal was calculated using the calculation shown below:

$$\Delta z = h_0 - hf$$

Assuming  $h_0$  is the millimeter-based initial height. High frequency is the after the test thickness in mm of a comparable object that has

not been corroded by seawater, and  $z$  is the metal's initial thickness drop in meters.

#### *Cast Fe-30Mn-1C alloy*

Fe-30Mn-1C alloy rods that had been cast were converted to a 7 mm diameter, cut into discs with a 5 mm thickness, and then covered with epoxy resin. Fe, Mn, and 316L samples were also made in a similar manner. Each sample's two disc faces were washed with ethanol, and then mechanically ground using SiC paper up to grit 4000 before being dried in the air. These samples acted as working electrodes with rotating discs. They were fastened to an electrode rotor with a rotational speed of up to 10,000 rpm, the EG&G Parc Model 616B. Metal springs were used to conduct the electronic contact between the instrument and the sample's back face. To create laminar flow conditions for the test medium, a 500-rpm rotational speed was used. The



electrochemical cell was coupled to a Solectron SI 1287 electrochemical interface and included a Pt net as a counter electrode and a SCE reference electrode ( $E(\text{SHE}) = 0.241 \text{ V}$ ). The temperature was kept constant at  $37^\circ\text{C}$  for all measurements in a tempered double-wall glass cell in [Figure 5](#).

*We employed the following chemical test solutions*

1. SBF, which stands (Simulated Body Flow) developed adherence to Kokubo et al. including  $142 \text{ mM Na}^+$ ,  $5 \text{ mM K}^+$ ,  $1.5 \text{ mM Mg}^{2+}$ ,  $2.5 \text{ mM Ca}^{2+}$ ,  $147.8 \text{ mM Cl}^-$ ,  $4.2 \text{ mM HCO}_3^-$ ,  $1.0 \text{ mM HPO}_4^-$ , and  $0.5 \text{ mM SO}_4^{2-}$ ; the pH 7.45-7.6 was buffered with  $50 \text{ mM Tris}$  (Tris(hydroxymethyl)aminomethane,  $(\text{HOCH}_2)_3\text{CNH}_2$ ) and  $1 \text{ M HCl}$ .
2. The Steel Board of India a  $150 \text{ mM}$  (0.9%) sodium chloride solution that has been  $50 \text{ mM}$  Trinity pH-buffered is available from Sigma Aldrich. Tris-buffered saline (TBS) is a buffer used in certain biochemical techniques to keep the pH within a limited range. This formulation has an approximate sodium chloride concentration of  $150 \text{ mM}$  and a tris concentration of  $50 \text{ mM}$ . The pH of the buffer is adjusted to 7.6. TBS is frequently formulated with a detergent such as Tween-20 for staining applications such as Western blotting. As a surfactant, Tween-20's function is to dissolve the surface tension between the membrane and the solution, ensuring complete membrane surface area wetting.
3. NaCl: non-buffered treatments created with high-purity NaCl (Fa. Merck); in the first series with each other, pollutants with 150 millimetres of sodium chloride (N was prepared, and initial pH readings of 7.6, 5, 2, and 10 were adjusted with HCl and NaOH, as well; in the second series with each other, answers with  $150 \text{ mM}$ ,  $15 \text{ mM}$ ,  $1.5 \text{ mM}$ , and  $0.15 \text{ mM}$  NaCl were geared up, and a pH value of 7.6 (pH 10) was adjusted with NaOH. After monitoring the open-circuit voltage (OCP) for 1 h under circulating flow conditions, potentio flexible polarity observations were performed beginning with  $-0.15 \text{ V}$  vs. open circuit potential (OCP) up to an end peak potential of  $1.5 \text{ V}$  vs. the SCE using a potential scan rate of  $0.5 \text{ mV/s}$ . To assess the accuracy of

the data, each measurement was carried out a minimum of three times. The corrosion-related variables  $E_{\text{corr}}$  and  $i_{\text{corr}}$  were determined from the polarisation curves using the graphical Tafel extrapolation method. After anodic polarization testing and tests for corrosive under free corrosion circumstances (OCP, 4 hours), a few alloy samples were subjected to SEM studies with the goal to learn concerning the first corrosion steps using NaCl-based solutions for analyzing the degradation. Static immersion tests were carried out in  $450 \text{ ml}$  of SBF at  $37^\circ\text{C}$  for a variety of times (24 h, 72 h, and 168 h) for every combination samples in order to determine the mechanism governing Fe-30Mn-1C in the SBF solvent. Consequently, samples comprising the forged rod that were one and a half millimeters thick and 12 millimeters in length were cut out and ground to a 4000 SiC grit paper. ICP-OES was used to measure the metal release of Mn and Fe after impersistency (filtrate=dissolved fraction). Furthermore, the precipitate, or solid fraction, was dissolved in a hot solution containing  $5 \text{ ml}$  of hydrochloric acid (HCl),  $250 \text{ mg}$  of oxalic acid ( $\text{C}_2\text{H}_2\text{O}_4$ ), and  $5 \text{ ml}$  of distilled water in order to examine the solid corrosion products by ICP-OES. For each sample that was analyzed, the standard deviation of ingredient concentration of Fe and Mn was estimated through a four-fold measurement. The methodological error was therefore less than 1%.

Sputter depth-profiling X-ray photoelectric spectroscopy (XPS; Physical electronics PHI 5600 CI, Mg K radiation,  $400 \text{ W}$ ) was used to evaluate the alloy the weight of the sample outer layer coatings. Typical sensibility values for only one component were used to gauge space. As with immersion testing, one sample was subjected to SBF for an hour before being polished with  $0.25 \text{ mm}$  stone solution and ground to a 4000 SiC grit paper size for XPS analysis. Sputtering  $\text{Ar}^+$  ions ( $3.5 \text{ keV}$ ) at a rate of around  $3.3 \text{ nm/min}$  eroded a surface layer on  $\text{SiO}_2$ .

#### *Chemical characterization of Fe-30Mn-1C*

Characterizing the swiftly solidifying Fe-30Mn-1C alloy allowed for the identification of an austenitic material transition with Fm-3 m

structure. We demonstrate a microdendritic solid dendrite pattern.

*Biochemical degradation comparison experiments in SBF are TBS, which is and sodium chloride*

An early chemically phases of the alloy disintegration process in a simulated body fluid were evaluated using chemical polarity experiments with turbulent electrolytic flow. The austenitic Iron-30Mn-1C alloy's characteristic electrical density-potential curve was detected in SBF, which has a pH range of 7.45 to 7.6, after having been subjected for an hour under open circuit conditions. This alloy's two primary constituents, Fe and Mn, also showed up on the curve. Polarised contours have been generated in less complicated media in order to evaluate the effects of this medium's molecular complexity, ionic strength, and Tris buffer. These are 15 mM NaCl (pH 7.6) and TBS (150 mM sodium chloride, or 150 mM Tris buffered, pH 7.6). During anodic circumstances, the simple NaCl solution behaves as expected, with just a single sharp instantaneous density minimum afterwards a quick active dissolve. The phenomenon may thus be caused by the influence of the organic buffer Tris on the surface contacts of Fe. The early Fe reactions in Hank's solution, or SBF, were described as straightforward electrochemical oxidation to  $\text{Fe}^{2+}$  and subsequent competitive generation of  $\text{Fe}(\text{OH})_2/\text{Fe}(\text{OH})_3$ , or direct reaction with  $\text{Cl}^-$  to  $\text{FeCl}_2$ , which breaks down to  $\text{Fe}(\text{OH})_2$ . However, according to MacFarlane and Smedley, the dissolving process of Fe in chloride solutions under low polarisation circumstances is more intricate. It involves  $[\text{FeClOH}]$  ads being electrochemically adsorbate, being oxidised to  $\text{FeClOH}$  (a rate-determining step), and then being chemically broken lower to create  $\text{Fe}^{2+}$ . This can progressively deteriorate into  $\text{Fe}^{3+}$  when breath is provided. The chemical compound  $\text{Rs}(\text{hydroxymethyl})\text{aminomethane}$ , also known as Tris(II)- or Tris(III)-complexes, is the subject of the acronym Tris. This complex synthesis might lead to distorted Fe solubility in tris-buffered chloride-containing liquids. Numerous minimum in the polarity curve point to the possibility that the Fe surface may have

momentarily disintegrated as a result of an increase in current density and a subsequent brief surface blockage (minima) brought on by an overabundance of low- or non-conducting contaminants [2, 6].

Thus, Fe absorption is inhibited across a broader possible variety. Only at greater anodic potentials-where the chlorine contributions are less significant-does the anticipated extreme active disintegrating activity occur. The nowadays density-potential patterns seen in Tris-buffered mixtures do not alter much when Mn and C are solved in austenite (-Fe). The Fe-30Mn-1C alloy has corrosion potentials that are comparable to the properties of the main component Iron but differ from those of Fe and Mn in each of the three test environments. Additionally, the density of corrosion currents are within the range that is typical for Fe, according to Leonardis and Mao *et al.* [5, 7]. Anodic polarization causes a significant increase in current density, which predicts strong alloy breakdown up to the mass transfer-controlled regime. The substantial responsiveness of Mn has been demonstrated to counteract the effect of the probable Fe-complex formation mentioned above, which might explain why alloy dissolving in Tris-buffered solutions didn't exhibit any anomalies. However, it was shown in a previous study that combining C with Fe (Fe-1C) can also have this effect. According to Chiaberge *et al.*, Esih and Fang [13- 15].

As a whole, it seems as though the chemistry of such an austenitic alloy Fe-30Mn-1C alloy is significantly reduced susceptible to the effects of the Tris buffer when compared with pure iron. However, in light of the aforementioned events, the usage of manufactured synthetic buffering like Tris should be seen as essential to study the decomposing reactions of the innovative biodegradable metallic materials. These might be explained by the complex solution structure, which includes anions, which are like  $\text{HCO}_3^-$  dissolves and  $\text{HPO}_4^-$ , which can cause salt formation, impede the dissolution of metals brought on by chloride, and have buffering effects, as mentioned by Karplus and McCammon [1].

Competitive experiments on 316L steel were also carried out to underline the austenitic alloy's reactive character. Compared to the degradable alloy, the relevant weathering current concentrations for 316 L are 1 to 3 orders of magnitude lower, and the risk of corrosion values are typically the highest positive values. Due to the high levels of Cr and Ni in the writing material, which allow the steel surface to spontaneously passivate and so stop dissolving processes, this predicts very low acidity. Anodic polaris causes a sharp increase in electricity density, which is followed by an inert plateau before pitting begins.

Regarding near-neutral water-based solutions, the water-soluble hydroxides that  $\text{Fe}(\text{OH})_2/\text{Fe}(\text{OH})_3$  and  $\text{Mn}(\text{OH})_2$  may create, perhaps as a consequence of the dissociation of metal-chloro combinations or by direct interaction of the dissolved ionic metal species with formed hydroxide ions, are essentially stable. The finding of Ca and P species on the surface area is additional proof that phosphate compounds are precipitating at this early stage of immersion. Moreover, C species linked to the production of carbon dioxide chemicals and pollution of the outer most area may be seen.

#### *Hydroxide measure concentration and micro structure*

The essential components and phases of the outcomes of corrosion were characterized using SEM and XRD methods. The chemistry of the materials and microstructural inspection of the cross-sectional characteristics of the oxidation scales were performed through a FESEM, or featuring Electricity Dispersive. The use of spectrum (EDS) (Oxford The devices INCA-350 framework, Abingdon, UK) to determine the protective qualities of the oxide strategies set up

on the alloys of stainless steel (120, 300, then 700, and 1000 h).

Experimental horizontal samples have been created for the metallographic analysis by being ground and polished with diamond suspensions of progressively smaller particle sizes (30-6-3 m), after their embedding in a phenolic resin material (Buehler, Lake Bluff, IL, USA).

X-ray diffraction techniques (Bruker, D8-Advance, Billerica, MA, USA) and Cu K radiation (operated at 40 kV and 40 mA) were used to determine the crystalline components of the iron scales (Table 1).

Bruker AXS's Diffrac Plus EVA software and the JCPDS database were used to conduct phase identification.

#### *Scratch test*

Contact examinations were performed to evaluate the oxide scales' stiffness and their adhesion to the substrate. A scratched tester (CSM Instruments Revetest, Needham, MA, USA) with a 200 m-radius Rockwell C diamond indenter was used. A 5 mm scratched height and a gradually increasing load from 0 to 80 N at a constant loading rate of 100 N/min were used for the experiments. Later, deterioration and malfunction could be seen thanks to microscopy with optical fibers.

#### *Profilometry test*

Employing a contact-based profilometer (Dektak 150 Stylus, Bruker, Billerica, MA, USA), the whole topographical characteristics and the external roughness index (Ra) associated with the oxide scales were evaluated at three distinct points on each sample.

Three mm were scanned using a point with a radius of 50 nm and an impact force of five milligrams. The Stylus software provided the surface roughness parameter (Ra). Ra was

**Table 1:** Atomic structure of steel molecules

Steel	Fe	Cr	Ni	Mo	Mn	C	N	Si	P	S
SS301	Bal.	17.4	7.2	0.1	1.2	0.02	0.12	<1.0	<0.03	<0.006
DS2205	Bal.	22.6	5.2	3.0	1.5	0.02	0.16	<0.45	<0.03	<0.015
DS2507	Bal.	25.0	7.4	3.8	2.0	0.01	0.24	<0.8	<0.03	<0.015

**Table 2:** Comparison between SS 301, DS2205, and DS2507 steel

	SS301	DS2205	DS2507
CR(mm/year) from 0 to 300 h	0.69	1.02	0.59
CR(mm/year) from 700 to 1300 h	0.22	0.29	0.17

calculated for each value and its standard deviation from at least three different areas of each sample.

#### *Corrosion resistance*

A potentiodynamic approach was used to conduct the experiments in accordance with standard procedure. The experiments' electrolyte microenvironment was chosen to reflect the majority of typical risks under the conditions of a potential layer implementation. A strong solution of sulfuric acid at an acidity level of 3.5 was used for the testing. The measuring potentials, when assessed towards the fully saturated monitoring the electrodes, ranged from -1 V to +0.8 V for each of the solutions. A platinum wire was used as the counter electrode for the tests, which were conducted in a round detecting cell of model A-011951. The Galvano stat ATLAS 0531 gadget was used to determine intensities caused by electricity and to detect potential variations at an acceleration of 1 mV/s. The computer programmer ECLAB version 10.37, Science Instruments, from Bio-Logic Company was used to compile the measurement findings. The following corrosion process parameters were established for each measurement based on the anode and cathode coefficients of the slope of straight lines that follow Tafel's law: The potential of the calomel electrode was taken into consideration while calculating the values shown below. The potential values of layer breakdown  $E_{\text{breakdown}}$  [mV], where a sudden increase in the intensity of the observed currents occurred, were determined by raising the potentials higher than the values of the equilibrium potentials of Tafel cathode and anode processes (Table 2).

This implies that how much of layer cracking, the measurement of the cracks, and the number of gaps are of lesser significance because as soon as the electrolyte contacts the substrate and anode potentials rise, corrosion events are started that

are limited to control by the substrate's corrosion resistance, which in this case is mainly dictated by the amount of chromium bonded in the oxide the passivation procedure.

## **Results**

#### *Corrosion rates*

Molybdenum and chromium concentrations also helped to provide greater corrosion resistance and a slower rate of corrosion. The oxidation process occurred quite rapidly in the initial a number of hours of exposure before dropping to lower levels beyond that point, as evidenced by the fact because the loss thickness tendency did not appear linear. The next set of figures illustrate the progression of the thickness degradation for the three steels as an indicator of time spent in contact with the molten salts. The dimension loss of the alloys increased in the following sequence in molten carbonate sodium salts at 600 °C: DS2507, SS301, and DS2205.

The tables below show that the nickel content of the tested steels is mostly responsible for improving their corrosion resistance. In this regard, DS2205 had a greater thickness loss (5.2 Ni wt%) than did DS2507 and SS301, which had 7.4 and 7.2 Ni (wt%), respectively. The ability to resist corrosion of DS2507, however, is higher than that of SS301 (25.0 Cr wt% and 3.8 Mo wt%) (17.2 Cr wt% and 0.1 Mo wt%). The information below shows that the higher corrosion resistance of the evaluated steels is mostly attributable to their nickel content. DS2205 showed a greater thickness loss (5.2 Ni wt%) than DS2507 and SS301, whose had thickness losses of 7.4 and 7.2 Ni (wt%), respectively. However, DS2507 has better protection against corrosion than SS301 (25.0 Cr wt% and 3.8 Mo wt%) and 17.2 Cr wt% and 0.1 Mo wt%). SEM external surface of steel showed in Figure 3.



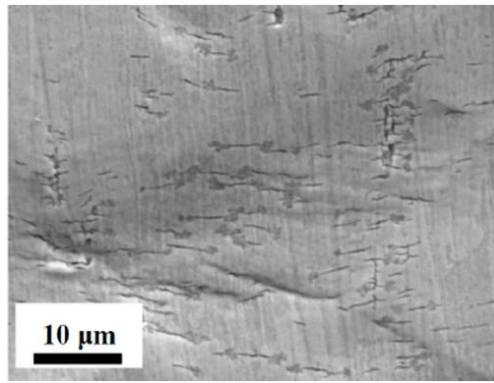


**Figure 3:** SEM external surface of steel

This kinematics formula which suggests a certain restrictions on cation transport at the oxide scales may be used to determine the efficiency of the shielding oxide layers created during the deterioration experiments [Figure 4](#).

The inclination of inclination of the loss depth curves at the starting points between 0 and 300 h

and between 700 and 1300 h, as shown in the figures was used to compute the initial corrosion velocity. [Figure 5](#) displays the corrosive rates for each steel that was exposed to molten salts of carbonate at 600 °C.

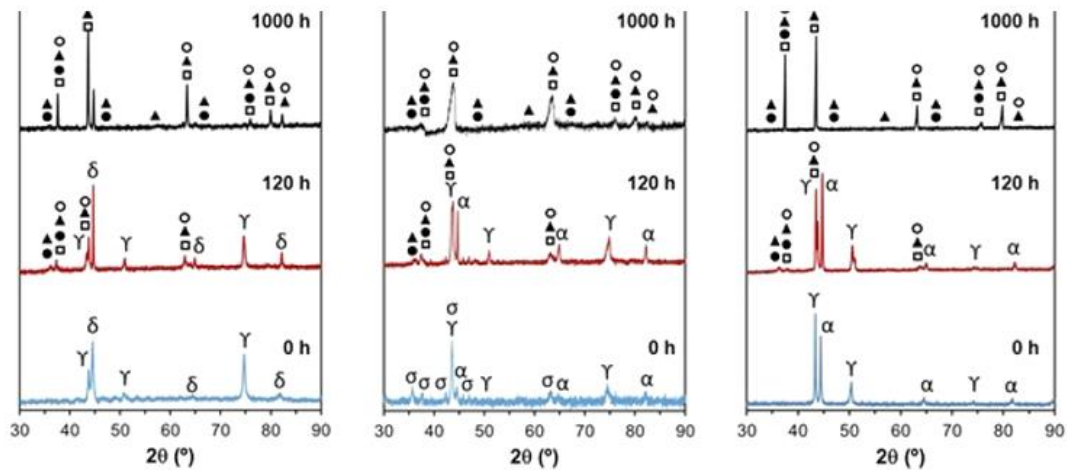


**Figure 4:** Peak identification chart

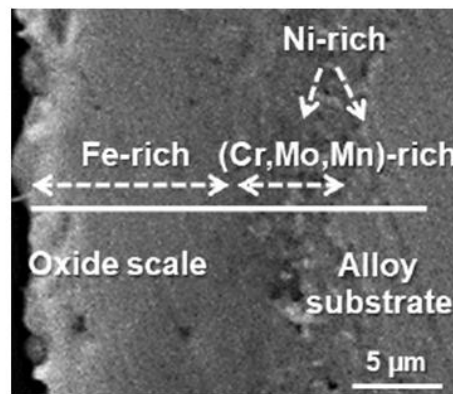


**Figure 5:** Oxide scale alloy substrate

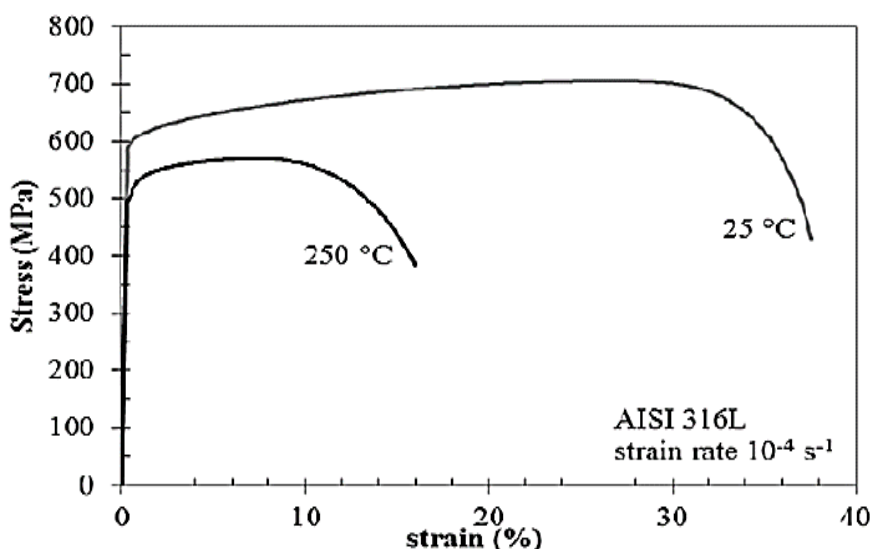


**Figure 6:** Stress strain curve

Owing the production of protective oxide levels, the stainless steels used in this research only had little oxidation between 400 and 500 °C, whereas stainless steels tended to experience linear oxidation and severe corrosion at temperatures in excess of 600 °C [Figure 6](#).

The austenitic alloy the metals of steel made from stainless steel, the majority of which contain nickel, exhibit significantly higher a high temperature strength compared with other alloys, it has been predicted that the AISI 316 stainless steel, which has not only a higher Ni information than the SS301, DS2205, and 2507, but less Chromium, also and Molybdenum than duplex alloys, will corrode at rates between 0.22 and 2.07 mm/year when exposed to various nitrogen oxide salt statements at 600 °C. Shown in [Table 3](#) and [Figure 6](#).

*Oxidation scale composition and structure that occurs*

The XRD data for the oxidation plates SS301, DS2205, and DS2507 after 120 and 1000 hours

of exposure to molten salts. The XRD characteristics for the steels provides-received (before to corrosion trials) are also supplied as an example of reference to help distinguish between the unique structures of each alloy as well as of the aluminum oxide scales.

The aluminum oxide layers revealed layers that were both smooth and compact, but they also revealed faults like holes, voids, and vertical grooves that were near to the borders and where the inner oxide layers intersected. The creation of corrosion products, particularly  $\text{LiFeO}_2$ , as well as the SS301, DS2507, and DS2205 oxide scales, may be related to the formation of pores and voids. In addition, DS2205 demonstrated internal breakdown, distinct segregation of the outer oxide scales in certain locations, partial delamination at the interface between the inner and external layers, as well as other flaws. Because of the DS2205's lower Ni content, permeability and other faults like them may

**Table 3:** Comparison of results of AISL 316,304 L

Material	Strain Rate ( $\text{s}^{-1}$ )	Position Specimen's Gauge Length	Waiting Time ( $\text{h}^*$ )	IA%	IZ%
	$10^{-5}$	Liquid phase	0	4	26
			55	21	10
AISI 316L		Gas phase	0	25	27
	$10^{-6}$	Liquid phase	0	21	12
		Gas phase	0	21	20
AISI 304L	$10^{-5}$	Liquid phase	0	38	37

develop more quickly as well as corrosion. The results shown are the oxidation scales' height and morphology after a 1000-hour period. The same-period corrosion rates indicate that all steels have experienced this corrosion layer detachment process, according to this premise. The distribution of these compounds inside the multifaceted oxide scale frameworks will be examined using SEM. However, due to lithium's low molecular weight, which precludes it from being recognized by scanning electron microscopy (SEM), the production of Li-containing compounds from corrosion has only been investigated using XRD. The as-received steels for SS301 displayed different stages and, followed by those for DS2205, DS2507, and DS2507. Each of three steels was found to include the oxide scale peaks for the chromium oxides (such as  $\text{FeCr}_2\text{O}_4$  and  $\text{LiCrO}_2$ ), iron oxides (such as  $\text{LiFeO}_2$ ), and nickel oxide ( $\text{NiO}$ ) after the two types of alloys were exposed for a total of 120 hours.

Yet, the amount of them did grow with prolonged exposure since steels treated for 120 h had an increase in their relative peak intensities. After 1000 h, no apparent change in the composition of the oxide phases was seen. Li-containing corrosion products, such as  $\text{LiFeO}_2$  and  $\text{LiCrO}_2$ , were discovered in the oxidation scaling of each of three stainless steels, which was in excellent

agreement with past study observed for other austenitic stainless steels in a comparable environment.

#### *Mechanical durability of oxides layers*

Overall, robust mechanical strength of the oxide scales and their adherence to the metallic substrate are connected to resistant to corrosion, especially in melted salts, where they may be prevented from separating during usage and the rate of slowed corrosion. To ascertain their mechanical integrity and stickiness, it is appropriate to analyze the scratch test tracks. The percentage of gaps and small cracks in each alloy subjected for 120 hours and 1000 hours was similar, maintaining the mechanical integrity of the oxide scales throughout time. While an oxide layer and bottom layer lived together in the scratch valley, both samples after 120 hours and 1000 hours revealed a progressive removal of the oxide coating lacking DE cohesion at the scale-substrate junction at the intermediate location of the scratch. According to this failure mechanism, every one of the steels' oxide scales had strong adherence to the metals substrate. These outcomes therefore matched the oxide scale flaws quite well. These findings therefore matched the oxide scale flaws quite well (Figure 7).

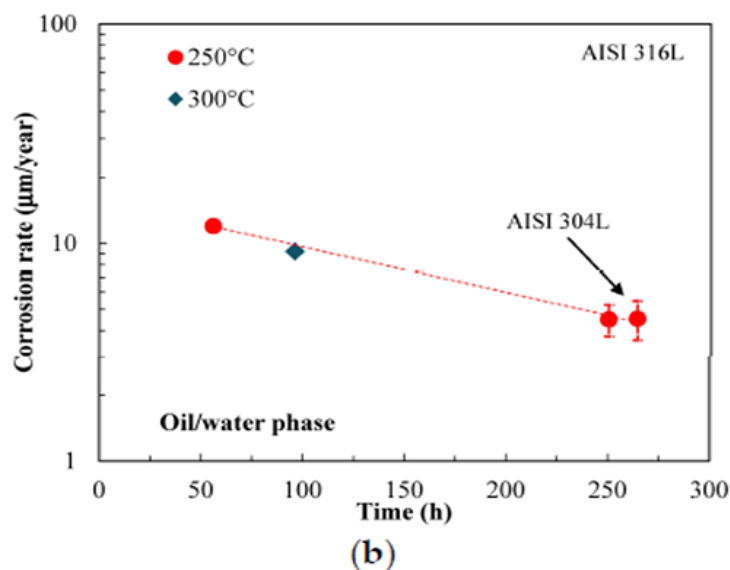


**Figure 7:** Corrosion rates



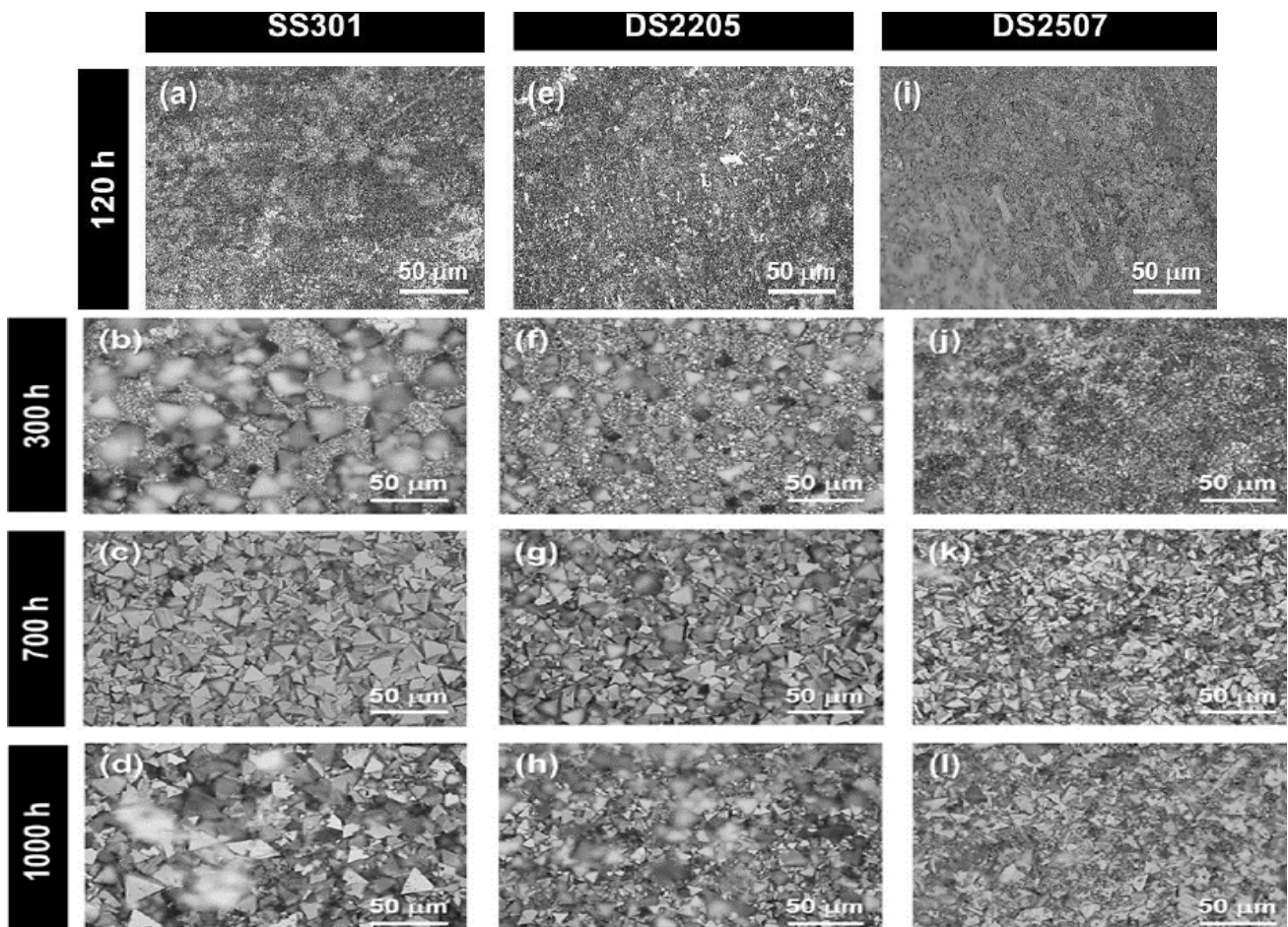
### Oxide granules' structure on the surface

Figure 8 showed the surface topography of the oxide scales may be a significant issue for the future usage of these steels in CSP facilities. This causes a certain degree of friction between the metal surface and the salt when the hot salts circulate throughout various regions of the CSP-like pipes, tanks, and tubes. The detachment of oxide scales under operation may be impacted by both weak and severe smooth of the exterior, which can enhance the friction between the oxide scale and molten salt. After all of the specimens were subjected to molten salts for 120 hours, 300 hours, and 700 hours, top surface images of the metal scales were taken using the optical microscope technique. It was found that as the exposure time in molten salt increased, the size of the crystallographic oxide scale grains for each alloy continuously increased.

Movements in the humid gas phase over the experiment period average around 10 m/year, and the total attack is modest. At 300 °C, the

values just slightly rise. Although water and oil phase corrosion rates are comparable to gas phase rates, they tend to decrease with time at a rate of around 5 m/year. Only tests with AISI 304L steel were performed, and only at 250 °C. Although the surface pits of AISI 304L stainless steel were deeper and widened, both AISI 316L and AISI 304L steels exhibited identical rates of corrosion.

Cracking caused by stress corrosion was not visible on the U-bend sample. Binding cone microscopic cracks show that stress corrosion cracking only occurred during slower strain rate testing at stress greater than the anticipated yield toughness. The investigation of typical AISI 316L and 304L austenitic stainless steels under the air circumstances that result from the process of dewatering of the organically sorted portion of solid waste from cities is the study's ultimate objective. Cracking test showed in Figure 9.



**Figure 8:** Surface test corrosion of steels



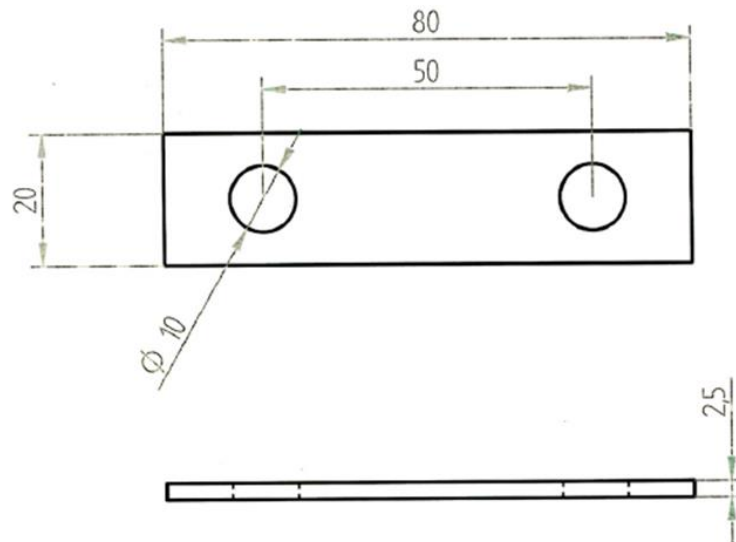


**Figure 9:** Cracking test

Throughout testing, colored oxide coatings underneath carbonate scales were discovered in all U-bend specimens. These layers ranged in color from metallic grey to black-brown while also displaying shades of bronze, gold, purple, red, blue, among green. Given that film hues on the metal interfere with one another, a change in color denotes a thicker deposit in [Figure 8](#).

Energy Dispersive Spectrometer (EDS) analysis results revealed a transient decrease in iron and a rise in chromium and oxygen, indicating that copper oxide made up the majority of the oxide layer showed in [Figure 10, 11](#).

Strengthen weathering Metallographic slices of U-bend specimens and ocular examinations of exposed surfaces were used to assess cracking.

The samples showed no signs of fracturing. Only minuscule faults on slip bands with a 20 m depth limit were observed. AISI shallow pit showed in [Figure 12](#).

The fracture is caused by the coalescence of numerous cracks on the specimen's surface, which results in a noticeably lower value for ductile parameters, primarily the area. The cracks have brittle development and the usual chloride SCC appearance. Their surface expansion is restricted to less than 150 m. On the necking cone's surface, secondary cracks with a similar morphology were also visible. Numerous small cracks have also been found further from the necking because to the work hardened caused by the machining of the specimen in [Figure 13](#).

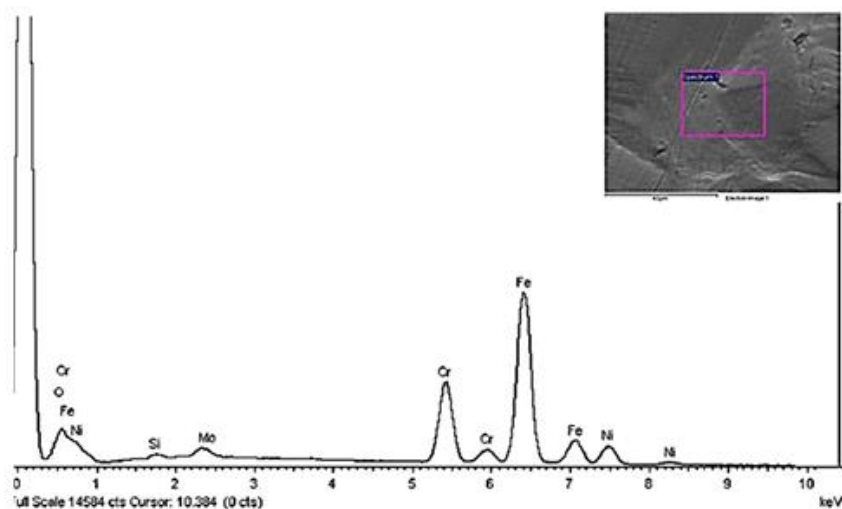


**Figure 10:** EDS analysis

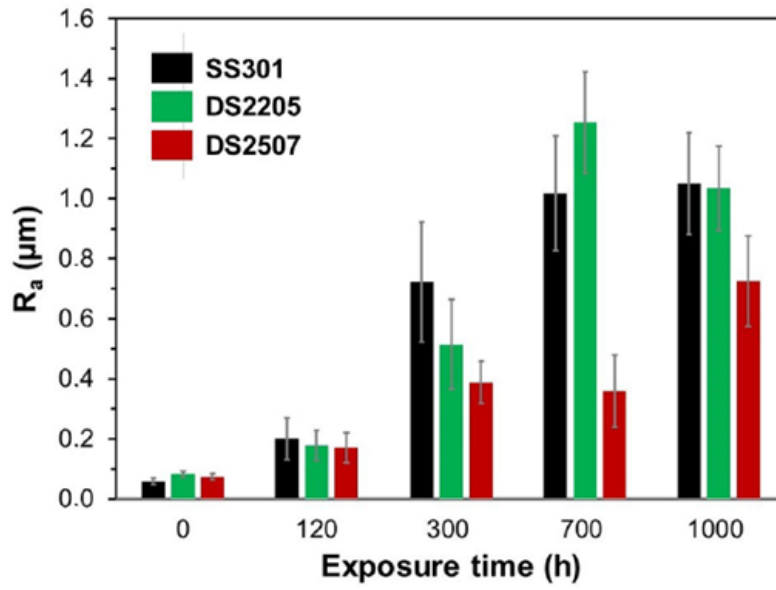


Figure 11: Surface parameter histogram

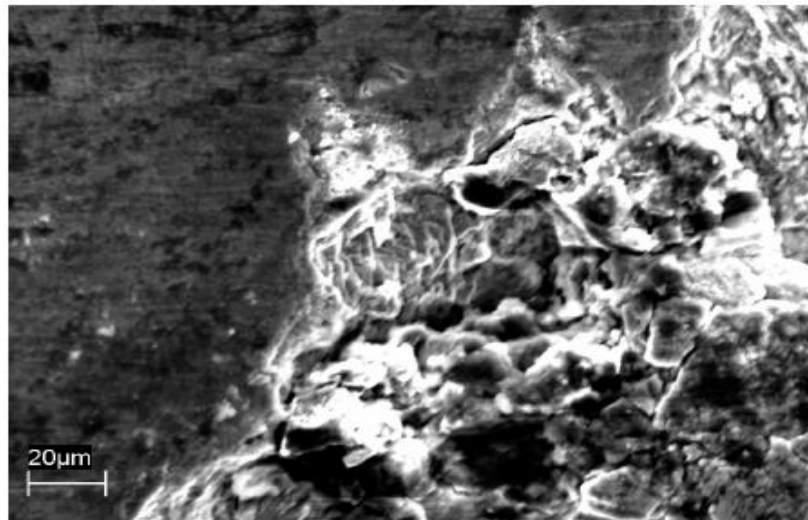


Figure 12: AISI shallow pit

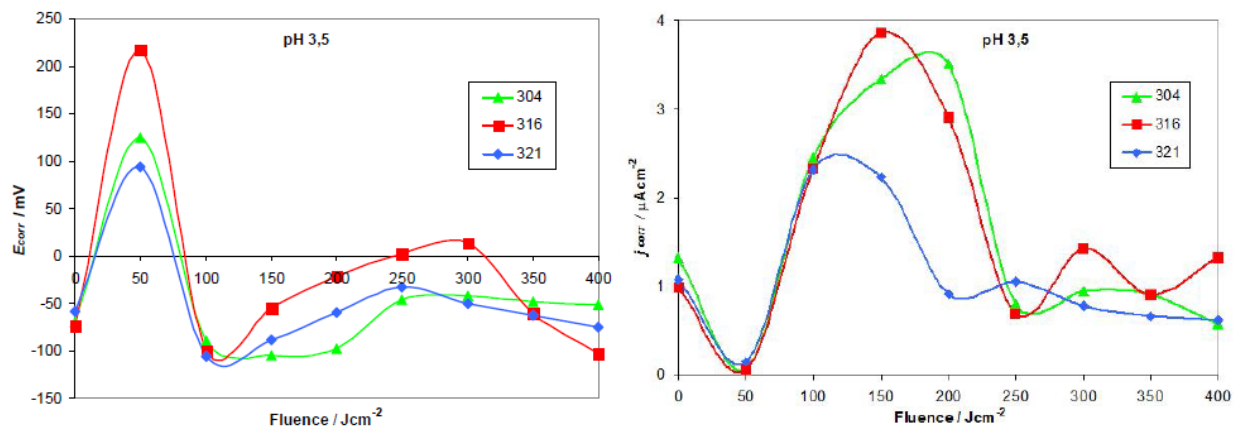
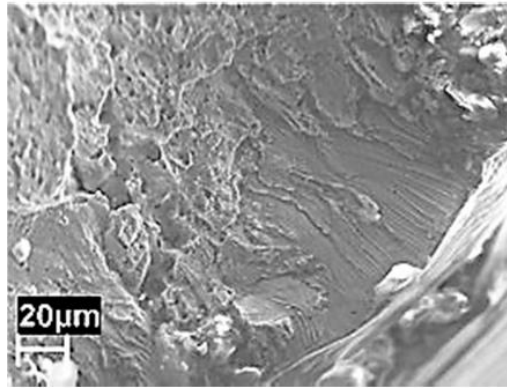
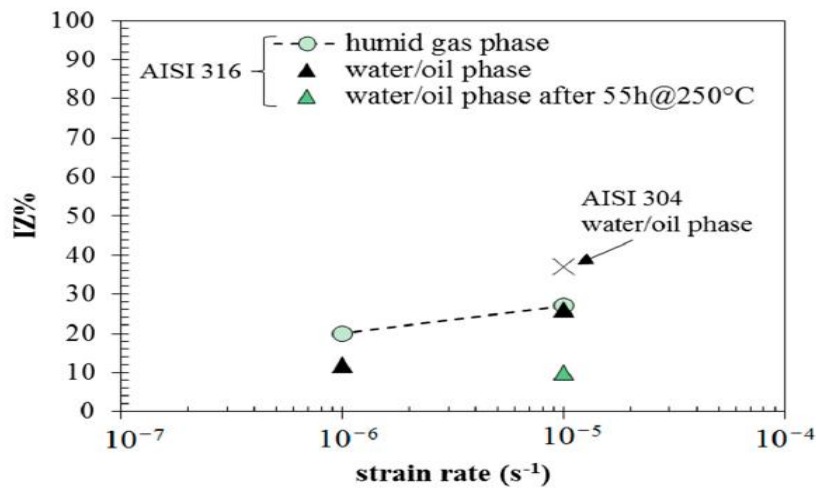


Figure 13: Potentioelectric curves



**Figure 14:** AISI steel's structure following an SSR examination



**Figure 15:** Embrittlement study

The material's surface fractures merge to form a crack, which results in a noticeable decline in ductile characteristics.

The strain-hardening process of stainless steels made from austenitic alloys at high temperatures, which limits the degree of homogeneous plastic deformation, promotes the early appearance of the necking process. The specimens examined in air really exhibit entirely fractured ductility surfaces. The fracture surface at 25 °C shows a ductile shape that is typical, with little dimples. At 250 °C, transversal ductile separations may be seen and the dimples grow larger showed in [Figures 14 and 15](#).

## Discussion

The findings demonstrate that both regional corrosion and SCC are substantially less likely to occur in the two austenitic stainless steels during the batch liquefaction process. In any event, very low corrosion rates discovered during tests

should be disregarded. In fact, due to the creation of a passive layer made of chromium-rich oxide, common austenitic stainless steels like AISI 316L and AISI 304L steels offer good general-purpose corrosion resistance. In the liquid phase, the protective layer is stable across a broad pH range. Pitting corrosion was not particularly evident despite the high temperature (240-300 °C) and high chloride concentration (400-5000 mg/L) in the water stage. Only AISI 304L steels had significant chipping; it only sometimes spread. These findings concur with those of Ruletue and Roy and Chiaberge *et al.* [8, 9] Pitting typically takes place in an oxidant presence when conditions are favourable for corrosion potentials that are high enough to outweigh the pitting potential. Passive stainless steel's corrosion potential is primarily influenced by how oxidising the environment is. In reducing conditions compared to oxidising ones, it is significantly lower. Otherwise, the concentration of chlorides,

the pH, and the solution's temperature all affect the pitting potential. Due to its brief length and changes in the environment during the initial stages of the liquefaction reactions, the batch procedure results in minimal corrosivity. Soon after starting in the batch procedure for coagulation, the addition of dissolution of oxygen fosters an oxidising microenvironment that is favourable for pit start. Oxygen deprivation also slows the spread of shallow holes that were started in the early stages. Because of the high temperature and pressure involved in batch liquefaction, it is very challenging to determine the dissolved oxygen content. Temperature processing results in a number of various processes, primarily DE monomer and consolidation with a wide range of adverse consequences. The reaction's effluent contained light hydrocarbons including CH<sub>4</sub>, ethane, and propane as well as stable gases like H<sub>2</sub>, CO, and CO<sub>2</sub>. The aforementioned products demonstrate the existence of radical-forming processes (cracking reactions). As soon as the temperature hits 220-240-C, these processes begin. Additionally, oxygen is a catalyst for radical processes, and its existence results in oxygen being completely scavenged. These results were in agreement with Di Yadav and Trasatti *et al* [10,17]. The data show that there is a chance of corrosion when oxygen is present for a long time. Selecting stainless steel grades with the appropriate molybdenum concentration thus seems more prudent. In addition, the characteristics of the protective coating affect the pitting potential. It is feasible to link the amount of weight loss seen during screening to the specimens' post-exposure color changes, which are solely dependent on the layer's thickness and degree of protection of the active movie. At temperatures more than 200 °C, the process of thermal oxidation causes semi-transparent oxide coatings to change color. The protective films are often too thin to employ the XPS method to detect changes in the element's concentration at temperatures below 400 °C, as mentioned by Greordon and Siniti [11, 12].

Thermal oxidizing considerably alters the passive monolayer of AISI 304L at temperatures between 150 and 300 °C in air, which favors the initiation

and growth of localized corrosion. Nevertheless, following batch coagulation, the sheet forms by chemical oxygenation under challenging and humid conditions, either on the section submerged or put in the gas phase. SCC was not clearly identified by tests on U-bend specimen; rather, only a few microdefects that developed in toughened zones were found.

-The measurable phenomena of SCC is rather small, despite the aqueous phase's considerable presence of chlorides as shown by chemical analysis.

Tugging plastic at extremely low rate of strain often improves chemically aided cracking events, as mentioned by Speidel [2].

For a long time electricity storage applications, the suitability of duplex stainless steels made up of grades 2205 and 2507 and austenitic stainless steel 301LN with eutectic Li<sub>2</sub>CO<sub>3</sub>-Na<sub>2</sub>CO<sub>3</sub>-K<sub>2</sub>CO<sub>3</sub> (32/33/35 wt%) molten salts was assessed. Steel corrodes in accordance with a parabola law. The rate at which corrosion occurs was calculated using the loss in metal thickness, and the values for SS301, DS2205, respectively DS2507, respectively, were 0.19-0.69, 0.22-1.02, and 0.17-0.59 mm/year. DS2507 displayed higher resistance to rust than SS301 and DS2205. The intermediate layer (LiCrO<sub>2</sub> and FeCr<sub>2</sub>O<sub>4</sub>) and the Ni-rich inner layer were separated by a narrow transition zone. It also revealed a Ni-enrichment at the inner layer for DS2507, as well as Cr enrichment, but a peak of Fe and a depletion of Cr for SS301 and DS2205, which may be the reason for DS2507's improved corrosion resistance. The innermost regions of oxide scales on the three metals such as steel nonetheless displayed outstanding adhesion to the metallic substrate. These results were in agreement with Liu et al [16]. The oxide scales of DS2507, however, featured a flatter oxide layer and a less rough surface as opposed to SS301 and DS2205.

## Conclusion

The percentage of the specimen's alteration in mass that m, at the area of the surface, S, as a function of immersion time, t, is shown as the losing weight rate, w, in Figure 2. The amount of weight loss, which is used to calculate the



corrosion rate of the steel, revealed that the inclinations of the curves were straight lines (correlation coefficient  $R^2$  are close to unity). The steel's wear rates are constant during the duration of the 48-hour soaking for each concentration of the chemicals C1, C2, and C3. Researchers looked at how temperature affected the effectiveness of C1, C2, and C3 chemicals as inhibitors. In a solution containing 0.5 M HCl, C3 outperforms C2 and C1 in terms of steel corrosion inhibition. The activation energy levels increase when C1, C2, and C3 are joined, indicating a physical adsorption process. The rise in activation energy ( $E_a$ ) is caused by the considerable adsorption of these compounds at a specific temperature on the coated surface of stainless steel. In electrochemical studies, it was shown that the speed of laser radiation altered the deterioration resistance of particular colorful layers on each type of steel. Only AISI 304L steels displayed -pitting; there was no sign of spread. The bulk processing method's tendency to promote the development of reducing conditions may be primarily responsible for the decreased susceptibility to cracking. Only the plastic field under dynamic stress experiences SCC events. The microcracks were no deeper than 150 meters. Despite the aqueous phase's high chloride concentration (almost 5000 mg/L), oxygen depletion and the formation of an organic product deposit reduce the possibility of SCC through the liquefaction process. Following the SSR tests, weakening indices were calculated, and the results showed that AISI 316L steel had a little more resistance to SCC than AISI 304L steel.

## ORCID

Hala. M. Hassan

<https://orcid.org/0000-0001-7173-1095>

## References

- [1]. Keiser J.R., Howell M., Lewis S.A., Connatser, R.M., March. Corrosion studies of raw and treated biomass-derived pyrolysis oils. In *NACE CORROSION* (pp. NACE-2012). NACE. 2012 [Google Scholar], [Publisher]
- [2]. Speidel M.O., Stress corrosion cracking of stainless steels in NaCl solutions. *Metallurgical Transactions A*, 1981, **12**:779 [Crossref], [Google Scholar], [Publisher]
- [3]. Brady M.P., Keiser J.R., Leonard D.N., Whitmer L., Thomson J.K., Corrosion considerations for thermochemical biomass liquefaction process systems in biofuel production, *JOM*, 2014, **66**:2583 [Crossref], [Google Scholar], [Publisher]
- [4]. Ding W., Bauer T., Progress in research and development of molten chloride salt technology for next generation concentrated solar power plants, *Engineering*, 2021, **7**:334 [Crossref], [Google Scholar], [Publisher]
- [5]. Mao Q., Zhang L., Wu H., Liu X., Design and calculation of a new storage tank for concentrating solar power plant, *Energy Conversion and Management*, 2015, **100**:414 [Crossref], [Google Scholar], [Publisher]
- [6]. Cabrini M., Lorenzi S., Marcassoli P., Pastore T., Hydrogen embrittlement behavior of HSLA line pipe steel under cathodic protection, 2011 [Crossref], [Google Scholar], [Publisher]
- [7]. Leonardis I., Chiaberge S., Fiorani T., Spera S., Battistel E., Bosetti A., Cesti P., Reale S., De Angelis F., Characterization of bio-oil from hydrothermal liquefaction of organic waste by NMR spectroscopy and FTICR mass spectrometry, *ChemSusChem*, 2013, **6**:160 [Crossref], [Google Scholar], [Publisher]
- [8]. a) Aubin H., Roy C., Study on the corrosiveness op wood pyrolysis oils, *Petroleum Science and Technology*, 1990, **8**:77 [Crossref], [Google Scholar], [Publisher] b) Brindred S., Akhtarian Zand M., Improve the Transient Stability of the Power Network Using STATCOM, *Eurasian Journal of Science and Technology*, 2021, **1**:104 [Crossref], [Publisher] c) Karimi M., Review of Steel Material Engineering and Its Application in Industry, *Journal of Engineering in Industrial Research*, 2023, **4**:61 [Crossref], [Publisher] d) Emelu V. O., Emelu C., Babatunde B. B., Wali E., Afolabi O. O., Associated Disaster Risk of Inadequate Corrosion Control (Cathodic Protection) on Pipelines in Port Harcourt, Nigeria: A Quantitative Approach, *Journal of Engineering in Industrial Research*, 2023, **4**:22 [Crossref], [Publisher]
- [9]. Cabrini M., Lorenzi S., Pastore T., Pellegrini S., Burattini M., Miglio R., Study of the corrosion resistance of austenitic stainless steels during conversion of waste to biofuel. *Materials*, 2017, **10**:325 [Crossref], [Google Scholar], [Publisher]

- [10]. Di Iorio C., Cheldi T., Correria S., LoPiccolo E., Mortali G., Evaluation of environmentally friendly corrosion inhibitors vs. traditional corrosion inhibitors in oil and gas industry. In Proceedings of the Eurocorr. 2014 [[Google Scholar](#)]
- [11]. Greordon, B. The effect of chloride and oxygen on tie stress corrosion cracking of stainless steels: Review of the literature. *Materials Performance*, 1980, **19**:29 [[Google Scholar](#)], [[Publisher](#)]
- [12]. Kuznetso Y.I., Organic inhibitors of corrosion of metals, Plenum Press, New York. 1996 [[Google Scholar](#)]
- [13]. Chiaberge S., Leonardis I., Fiorani T., Cesti P., Reale S., Angelis F.D., Bio-oil from waste: A comprehensive analytical study by soft-ionization FTICR mass spectrometry, *Energy & fuels*, 2014, **28**:2019 [[Crossref](#)], [[Google Scholar](#)], [[Publisher](#)]
- [14]. Esih I., Alar V., Juraga I., Influence of thermal oxides on pitting corrosion of stainless steel in chloride solutions, *Corrosion engineering, science and technology*, 2005, **40**:110 [[Crossref](#)], [[Google Scholar](#)], [[Publisher](#)]
- [15]. Fang J., Li J., Quantum chemistry study on the relationship between molecular structure and corrosion inhibition efficiency of amides, *Journal of Molecular Structure: THEOCHEM*, 2002, **593**:179 [[Crossref](#)], [[Google Scholar](#)], [[Publisher](#)]
- [16]. a) Liu M., Tay N.S., Bell S., Belusko M., Jacob R., Will G., Saman W., Bruno F., Review on concentrating solar power plants and new developments in high temperature thermal energy storage technologies, *Renewable and Sustainable Energy Reviews*, 2016, **53**:1411 [[Crossref](#)], [[Google Scholar](#)], [[Publisher](#)] b) Vaeli N., Laboratory Study of Effective Factors on How to Extract Carvacrol from Oliveria Decumbens Plant with the Help of Supercritical Fluid CO<sub>2</sub> and Using Ultrasound Waves, *Eurasian Journal of Science and Technology*, 2022, **2**:32 [[Crossref](#)], [[Publisher](#)] c) Akhtarian zand M., Optimization of corrosion information in oil and gas wells using electrochemical experiments, *Journal of Engineering in Industrial Research*, 2021, **2**:149 [[Crossref](#)], [[Publisher](#)]
- [17]. Trasatti S., Camona E., Mazza F., Sivieri E., Influence of the exposure of AISI 304L stainless steel at moderately high temperature on the susceptibility to crevice corrosion, *Journal of applied electrochemistry*, 1998, **28**:1333 [[Crossref](#)], [[Google Scholar](#)], [[Publisher](#)]

## HOW TO CITE THIS ARTICLE

Hala. M. Hassan\*. Evaluation of Several Austenitic Types of Stainless Steel's Chemical Corrosion Resistance. *Chem. Methodol.*, 2023, 7(11) 853-870

DOI: <https://doi.org/10.48309/chemm.2023.421394.1730>

URL: [https://www.chemmethod.com/article\\_183126.html](https://www.chemmethod.com/article_183126.html)